Binary hard-sphere fluids near a hard wall

R. Roth* and S. Dietrich

Fachbereich Physik, Bergische Universität Wuppertal, D-42097 Wuppertal, Germany

(Received 16 March 2000)

By using the Rosenfeld density functional, we determine the number density profiles of both components of binary hard-sphere fluids close to a planar hard wall as well as the corresponding excess coverage and surface tension. The comparison with published simulation data demonstrates that the Rosenfeld functional, both its original version and sophistications thereof, is superior to previous approaches, and exhibits the same excellent accuracy as known from studies of the corresponding one-component system.

PACS number(s): 61.20.−p, 68.45.−v

I. INTRODUCTION

A variety of experimental techniques has emerged which allow one to resolve the inhomogeneous density distributions of fluids at interfaces, a subject which enjoys broad scientific interest. In this context the ability to manufacture highly monodisperse colloidal suspensions has turned out to be particularly useful, as these provide the possibility to tune the effective interactions in these systems such that, e.g., the colloidal particles closely resemble hard-sphere fluids [1]. Since many of these experimental probes are indirect scattering techniques, there is a substantial demand to guide them theoretically. Computer simulations and integral theories [2] are important tools of statistical physics to address these issues. Density functional theory (DFT) [3] has emerged as an additional approach which is capable of capturing interfacial phase transitions and sweeping the thermodynamic and interaction parameter space of the system under consideration. The potential to combine these two possibilities poses a major challenge for other techniques. If DFT also acquires the same accuracy as the other two techniques, it could gain a clear competitive edge.

Although there is no recipe for systematically constructing a reliable DFT in spatial dimensions $d \geq 2$, the constant flux of developments over many years has led to a rather high level of sophistication. Among these theories for hard-sphere fluids, which act as paradigmatic systems and stepping stones for more complicated models, the Rosenfeld functional has emerged as a particular powerful theory which resorts to fundamental geometrical measures of the individual sphere [4]. For the standard test case of the highly inhomogeneous density distribution of a one-component hard-sphere fluid near a planar hard wall, the predictions of the Rosenfeld functional are very close to those of numerical simulations serving as benchmarks. For this case the mean square deviations [see, e.g., Eq. (22)] of Rosenfeld DFT results from the simulation data from Ref. [5] are at most 1 $\times 10^{-3}$ at high packing fractions, and otherwise less than 3 $\times 10^{-4}$.

Another virtue of the Rosenfeld functional is that is easily lends itself to generalization to multicomponent hard-sphere fluids. This opens the door to investigate rich new physical phenomena as particles of different size compete for interfacial positions [6]. Even for the simplest multicomponent system, the binary hard-sphere fluid, there are relatively few theoretical studies which determine their structural properties near a planar hard wall, using Monte Carlo simulations [7–10], integral equation theories [9], and various kinds of density functional theory [8–15], as well as in spherical pores [16]. Here we analyze this problem by using the corresponding Rosenfeld functional both in its original version [4] as well as for sophistications thereof [17,18]. By comparing these results with published simulation data [10], we assess to what extent the quantitative reliability of the Rosenfeld functional for the one-component hard-sphere fluid remains valid for the corresponding binary system. Moreover we determine concentration profiles, the excess coverage, and the surface tension of the binary hard-sphere fluids at a hard wall. We describe the DFT in Sec. II, and report our results in Sec. III, followed by a summary and our conclusions in Sec. IV. The Appendix contains important technical details.

II. DENSITY FUNCTIONAL THEORY

The Rosenfeld functional for the excess (over the ideal gas) Helmholtz free energy of a mixture of hard spheres with number density profiles $\{\rho_i(\mathbf{r})\}$, $i = 1, \ldots, N$, can be written as [4]

$$\beta \mathcal{F}_{ex}[\{n_\alpha\}] = \int d^3r \, \Phi(\{n_\alpha(\mathbf{r})\}), \qquad (1)$$

which is a functional of the four scalar weighted densities $n_\alpha(\mathbf{r})$ for the N-component mixture

$$n_\alpha(\mathbf{r}) = \sum_{i=1}^{N} \int d^3r' \rho_i(\mathbf{r}') \omega_i^{(\alpha)}(\mathbf{r} - \mathbf{r}'), \quad \alpha = 0, \ldots, 3, \qquad (2)$$

with $4N$ scalar weight functions $\omega_i^{(\alpha)}$ and two three-component vector weighted densities $\mathbf{n}_\alpha(\mathbf{r})$,

$$\mathbf{n}_\alpha(\mathbf{r}) = \sum_{i=1}^{N} \int d^3r' \rho_i(\mathbf{r}') \boldsymbol{\omega}_i^{(\alpha)}(\mathbf{r} - \mathbf{r}'), \quad \alpha = 1, 2, \qquad (3)$$

*Present address: H.H. Wills Physics Laboratory, University of Bristol, Royal Fort, Tyndall Avenue, Bristol BS8 1TL, U.K.

with $2N$ vector weight functions $\boldsymbol{\omega}_i^{(\alpha)}$. The weight functions contain *only* information about the fundamental geometrical measures of a single sphere of species i, namely, its volume, surface area, and radius R_i, i.e., in particular they are independent of the density profiles. The explicit expressions for the weight functions are given in the Appendix. $\Phi(\{n_\alpha\}) = \Phi_1 + \Phi_2 + \Phi_3$ is a function of the weighted densities, with [4]

$$\Phi_1 = -n_0 \log(1 - n_3), \tag{4}$$

$$\Phi_2 = \frac{n_1 n_2 - \mathbf{n}_1 \cdot \mathbf{n}_2}{1 - n_3}, \tag{5}$$

and

$$\Phi_3 = \frac{\frac{1}{3} n_2^3 - n_2 \mathbf{n}_2 \cdot \mathbf{n}_2}{8\pi(1 - n_3)^2} = \frac{n_2^3}{24\pi(1 - n_3)^2}(1 - 3\xi^2), \tag{6}$$

where $\xi(\mathbf{r}) \equiv |\mathbf{n}_2(\mathbf{r})|/n_2(\mathbf{r})$, which is the ratio of the modulus of the vector weighted density $\mathbf{n}_2(\mathbf{r})$ and the scalar weighted density $n_2(\mathbf{r})$. We note that $\xi(\mathbf{r}) \equiv 0$ in the bulk, and is small for small inhomogeneities. While this original Rosenfeld functional very successfully describes the fluid phase of a one-component hard-sphere system [19], it fails to predict the freezing transition. This failure was studied in detail in Refs. [17] and [18]. For the freezing transition it turns out that the zero-dimensional limit of the functional, in which a small cavity can accommodate only a single sphere, plays a key role. In a crystal the thermal vibrations around a lattice site can be interpreted as the motions in such a cavity formed by the neighboring spheres. Only if the statistical mechanics in such a cavity is described properly by the density functional can the freezing transition be predicted correctly. This is not the case for the original Rosenfeld functional. This problem can be fixed by slightly modifying the contribution Φ_3 [see Eq. (6)], such that the freezing transition is predicted by the modified functional while, at the same time, for lower packing fractions the accuracy of the original functional in describing the inhomogeneous fluid is kept. The following modifications have been suggested [17,18]:

$$\Phi_{3,q} = \frac{n_2^3}{24\pi(1 - n_3)^2}(1 - \xi^2)^q, \tag{7}$$

with $q \geq 2$, and

$$\Phi_{3,int} = \frac{n_2^3}{24\pi(1 - n_3)^2}(1 - 3\xi^2 + 2\xi^3). \tag{8}$$

The first suggestion, $\Phi_{3,q}$, is an antisymmetrized version of Φ_3 in Eq. (6), and the second, $\Phi_{3,int}$, interpolates between Φ_3 of Eq. (6) and $\Phi_{3,0D}$ in the exact zero-dimensional limit

$$\Phi_{3,0D} = \frac{n_2^3}{24\pi(1 - n_3)^2}\xi(1 - \xi)^2. \tag{9}$$

While the modified Rosenfeld function with $\Phi_{3,0D}$ successfully predicts the freezing transition of the one-component system, it leads to modified bulk properties, and hence can-

not describe the hard-sphere fluid as accurately as the original Rosenfeld functional. We note that the difference between Φ_3 of the original Rosenfeld functional and both $\Phi_{3,q}$ with $q = 3$ and $\Phi_{3,int}$ is of the order of $O(\xi^3)$. Therefore, we expect the largest differences between the various versions of the Rosenfeld DFT to occur close to the wall where ξ is largest.

Both the original Rosenfeld functional and the modifications corresponding to Eqs. (7) and (8), i.e., the functionals that share common bulk properties, are very successful and accurate for the one-component fluid. But far less is known for binary mixtures. In this latter respect, very good agreement between the density profiles obtained from the Rosenfeld functional and those obtained by simulation [7] was found in Ref. [20]. In a recent study [10], however, significant deviations between the Rosenfeld DFT results and simulations were found. In this latter study a density functional due to Kierlik and Rosinberg was applied [21], which has proven in general terms to be equivalent to the original Rosenfeld functional for any type of spatial inhomogeneity [22]. In order to demonstrate the equivalence of these functionals explicitly for a binary hard-sphere mixture close to a hard wall, we have performed calculations with both versions. The successful comparison of the corresponding results provides welcome reassurance in the general argument [22] and, in addition, serves as a valuable test of the reliability of our numerical procedures.

Here we are interested in the equilibrium density profiles $\rho_{s,0}(\mathbf{r})$ and $\rho_{b,0}(\mathbf{r})$ of both the small and big components of binary hard-sphere mixtures close to a planar hard wall. To this end we freely minimize the functional

$$\Omega[\rho_s(\mathbf{r}), \rho_b(\mathbf{r})] = \mathcal{F}[\rho_s(\mathbf{r}), \rho_b(\mathbf{r})]$$
$$+ \sum_{i=s,b} \int d^3 r' \rho_i(\mathbf{r}')(V_{ext}^i(\mathbf{r}') - \mu_i), \tag{10}$$

which is written in terms of the functional

$$\mathcal{F}[\rho_s(\mathbf{r}), \rho_b(\mathbf{r})] = \mathcal{F}_{id}[\rho_s(\mathbf{r}), \rho_b(\mathbf{r})] + \mathcal{F}_{ex}[\rho_s(\mathbf{r}), \rho_b(\mathbf{r})], \tag{11}$$

with the exactly known ideal gas contribution $\mathcal{F}_{id}$,

$$\beta\mathcal{F}_{id} = \sum_{i=s,b} \int d^3 r' \rho_i(\mathbf{r}')[\ln(\lambda_i^3 \rho_i(\mathbf{r}')) - 1], \tag{12}$$

with λ_i the thermal wavelength of species i. For the equilibrium density profiles $\rho_{i,0}(\mathbf{r})$, $i = s,b$, the functionals $\mathcal{F}$ and Ω reduce to the Helmholtz free energy and the grand canonical potential of the mixture, respectively; μ_s and μ_b are the chemical potentials of the two species. The external potentials entering into Eq. (10) model the planar hard wall at $z = 0$:

$$V_{ext}^i(z) = \begin{cases} \infty, & z < R_i \\ 0 & \text{otherwise.} \end{cases} \tag{13}$$

$i = s,b$, with z the normal distance from the wall. The external potentials prevent the centers of spheres of species i to approach the wall, located at $z = 0$, closer than R_i in which

case they are in contact. In the absence of spontaneous symmetry breaking due to freezing, which we do not consider here, the profiles $\rho_{i,0}(z)$, $i=s,b$, depend only on the normal coordinate z which simplifies the minimization of the functional.

Far away from the wall, i.e., in the bulk system, the vector-weighted densities $\mathbf{n}_1$ and $\mathbf{n}_2$ and thus ξ vanish. In this limit both the original Rosenfeld functional and the two modifications corresponding to Eqs. (7) and (8) reduce to the same bulk expression given by

$$\Phi_{bulk} = -n_0 \ln(1-n_3) + \frac{n_1 n_2}{1-n_3} + \frac{n_2^3}{24\pi(1-n_3)^2} \quad (14)$$

and hence they share the same bulk properties. We want to emphasize that as a consequence of this feature *all* versions of the Rosenfeld functional predict density profiles which show the *same* asymptotic decay toward the bulk value [23]. The weighted densities in the bulk limit are obtained by inserting the bulk densities $\rho_{i,bulk} := \rho_{i,0}(z=\infty)$ into Eq. (2), yielding

$$n_3 = \frac{4\pi}{3} \sum_{i=s,b} R_i^3 \rho_{i,bulk} \equiv \sum_{i=s,b} \eta_i, \quad (15)$$

$$n_2 = 4\pi \sum_{i=s,b} R_i^2 \rho_{i,bulk}, \quad (16)$$

$$n_1 = \sum_{i=s,b} R_i \rho_{i,bulk}, \quad (17)$$

and

$$n_0 = \sum_{i=s,b} \rho_{i,bulk}. \quad (18)$$

The equation of state following from Eq. (14),

$$\beta p = \frac{n_0}{1-n_3} + \frac{n_1 n_2}{(1-n_3)^2} + \frac{1}{12\pi} \frac{n_2^3}{(1-n_3)^3}, \quad (19)$$

is the Percus-Yevick compressibility equation of state of the mixture [24]. This expression is related to the contact values of the density profiles according to the sum rule [25]

$$\beta p = \sum_{i=s,b} \rho_i(z=R_i+0). \quad (20)$$

This sum rule is respected by the Rosenfeld functional as by any weighted-density DFT [26] and therefore provides a test of the numerical accuracy of the calculations. In the following we suppress the subscript 0, which indicates equilibrium profiles as opposed to variational functions.

III. STRUCTURAL AND THERMODYNAMIC PROPERTIES

A. Density profiles

The number density profiles of both components of binary hard-sphere mixtures close to a planar hard wall are obtained by a free minimization of the functional given in Eq. (10) using a conjugate gradient algorithm. The numerical accuracy of the resulting density profiles was affirmed by the fact that the functional derivative $\delta\Omega/\delta\rho_i(\mathbf{r})$, $i=s,b$, was always found to be zero within machine precision. We use the original Rosenfeld functional as well as the modified versions corresponding to Eqs. (8) and (7) with $q=2$ and 3. The systems considered here have two different size ratios, $R_b:R_s=5:3$ and $R_b:R_s=3:1$, and various packing fractions η_s and η_b for small and big spheres [27], respectively. The resulting density profiles are compared with simulation data published in Ref. [10]. In addition we calculate the local concentrations $\Phi_s(z)$ and $\Phi_b(z)$ of the small and large spheres, respectively, defined as

$$\Phi_i(z) = \frac{\rho_i(z)}{\rho_s(z)+\rho_b(z)}, \quad i=s,b. \quad (21)$$

We find excellent agreement between the density profiles of both components obtained by density functional theory and the simulation data for all systems under consideration. This holds for all versions of the Rosenfeld functional analyzed here. While at low total packing fractions $\eta=\eta_s+\eta_b$ the density functional theory results for all versions of the Rosenfeld functional are practically equivalent, small deviations among the results from different versions of the functional appear at larger values of η, i.e., for $\eta \gtrsim 0.3$. We quantify the degree of agreement between our DFT density profiles $\rho_i(z)$ and the simulation data from Ref. [10], available as data points $(z_j, \rho_i^{sim}(z_j))$, $j=1\ldots N_i^{sim}$ and $i=s,b$, by determining the mean square deviations $\bar{E}_i$, $i=s,b$, defined as

$$\bar{E}_i = \frac{1}{N_i^{sim}} \sum_{j=1}^{N_i^{sim}} \left(\frac{\rho_i^{sim}(z_j) - \rho_i(z_j)}{\rho_{i,bulk}} \right)^2. \quad (22)$$

We find that $\bar{E}_s$ and $\bar{E}_b$ are at most 5×10^{-4} and 6×10^{-3}, respectively, for all versions of the Rosenfeld functional. However, since the statistical errors in the simulation data are comparable with or even larger than the differences between the density profiles obtained by different versions of the Rosenfeld DFT, this approach does not enable us to determine which of the various versions is the most accurate one.

To illustrate the agreement between the DFT and the simulation data, in Fig. 1 we show the density profiles of the small spheres (a) and the big spheres (b) for $\eta_s=0.0607$ and $\eta_b=0.3105$ and a size ratio $R_b:R_s=5:3$. The symbols ($\square$) denote the simulation data from Ref. [10] and the solid line is obtained by the original Rosenfeld functional. The dotted lines denote coarse grained densities $\bar{\rho}_i^{(j)}$, $i=s,b$ and $j=0,1$, defined as

$$\bar{\rho}_i^{(j)} = \frac{1}{z_i^{(j+1)} - z_i^{(j)}} \int_{z_i^{(j)}}^{z_i^{(j+1)}} dz \frac{\rho_i(z)}{\rho_{i,bulk}}, \quad (23)$$

with $z_i^{(0)} \equiv 0$ and $z_i^{(j>0)}$ the position of the jth minimum [28]. All details of the density profiles found in the simulations are reproduced very accurately by the density func-
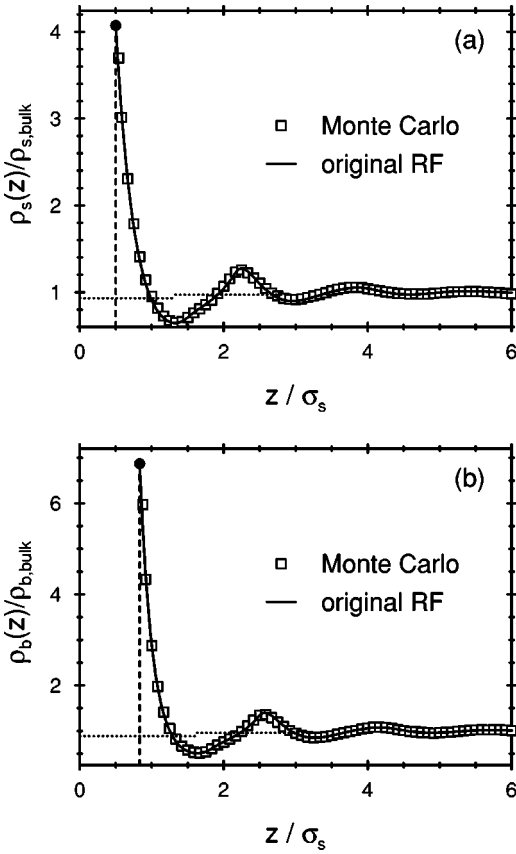
FIG. 1. The density profiles of the small spheres (a) and the big spheres (b) of a binary hard-sphere mixture with size ratio $R_b:R_s = 5:3$, and packing fractions $\eta_s = 0.0607$ and $\eta_b = 0.3105$ close to a planar hard wall (dashed line). $\sigma_s = 2R_s$ is the diameter of the small spheres. The solid lines correspond to results obtained by a free minimization of the original Rosenfeld functional, and the symbols ($\square$) denote simulation data from Ref. [10]. The full dots indicate the values at contact. The positions of the extrema of $\rho_s(z)$ and $\rho_b(z)$ are very close to each other if they are measured from the corresponding position of contact, i.e., $z = R_s = \frac{1}{2}\sigma_s$ and $z = R_b = \frac{5}{6}\sigma_s$, respectively. The dotted lines correspond to the coarse grained density profiles defined in Eq. (23). They indicate that in spite of the high contact values the wall actually leads to a slight net depletion for both species in the first layer.

tional theory. The oscillatory behavior, i.e., the amplitudes, phases, and decay of the oscillations as obtained by DFT, agree excellently with the simulations. The total packing fraction of the system $\eta = \eta_s + \eta_b = 0.3712$ is already rather high, giving rise to the pronounced structure of the density profiles. The corresponding concentration profiles $\Phi_s(z)$ and $\Phi_b(z)$ of the small and big spheres, respectively, are shown in Fig. 2. These concentration profiles demonstrate that, apart from the purely geometrical constraints, near the wall the big particles are enriched and the small particles are depleted. This is in line with the expectation based on the attractive depletion potential near a hard wall of a single big sphere immersed in a fluid of small spheres [30]. Correlation effects reverse this relative distribution in the second layer, and restore it in the third.

As mentioned above, small differences between the DFT results corresponding to the various versions of the Rosenfeld functional can be found for these values of η. In order to
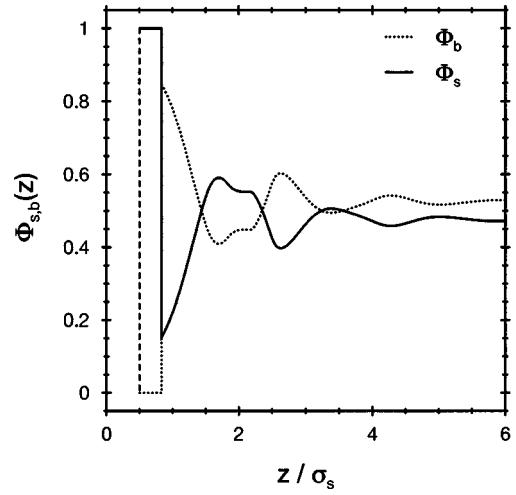

FIG. 2. The concentration profiles $\Phi_s(z)$ and $\Phi_b(z)$ of the small and big spheres, respectively, corresponding to the density profiles in Fig. 1. For geometric reasons $\rho_i(z \leq R_i) = 0$ with $R_s = \frac{1}{2}\sigma_s$ and $R_b = \frac{5}{6}\sigma_b$. Therefore, Φ_s and Φ_b are defined only for $z \geq \sigma_s$ and $\Phi_b(R_s < z < R_b) = 0$ and $\Phi_b(R_s < z < R_b) = 1$.
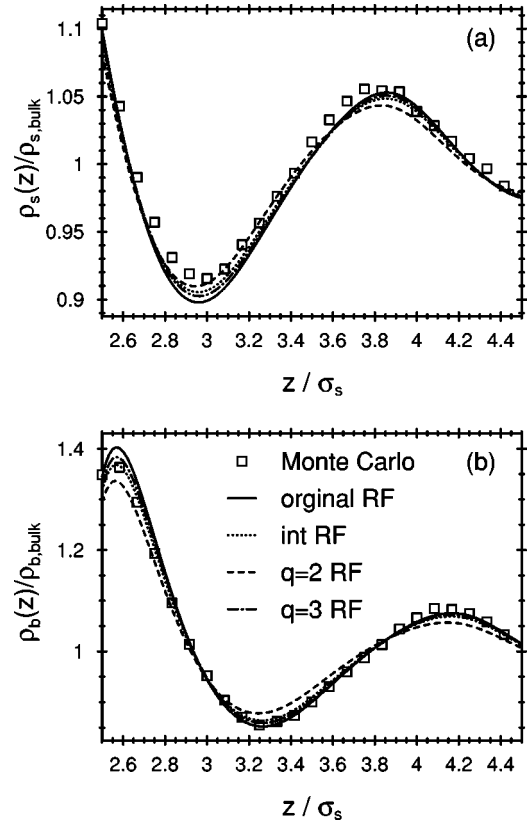

FIG. 3. In order to resolve the small differences in the density profiles of the small (a) and big (b) spheres between the DFT results obtained by the various versions of the Rosenfeld functional, parts of the density profiles shown in Fig. 1 are magnified here. The solid lines correspond to the original functional, whereas the dotted, dashed, and dash-dotted lines correspond to the interpolated version (int RF) and the antisymmetrized modification with $q = 2$ and 3, respectively. The parameters are the same as in Fig. 1.
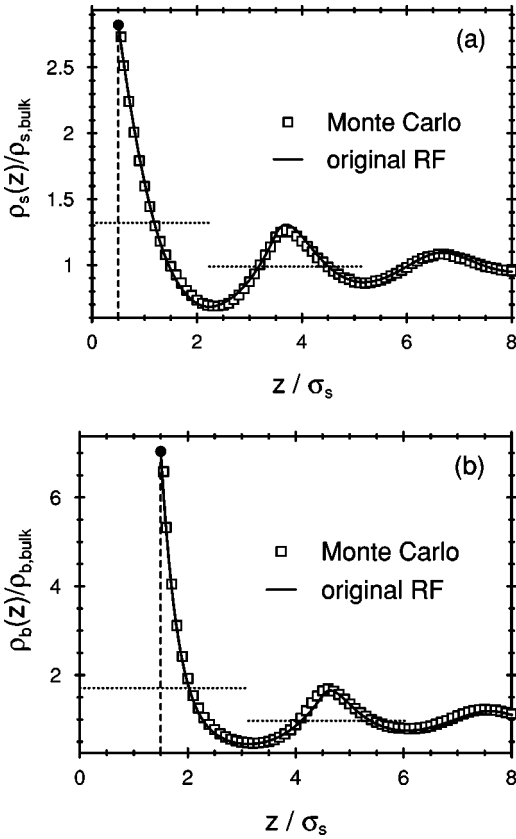
FIG. 4. The density profiles of the small spheres (a) and the big spheres (b) of a binary hard-sphere mixture with size ratio $R_b:R_s = 3:1$ and packing fractions $\eta_s = 0.0047$ and $\eta_b = 0.3859$ close to a planar hard wall. The solid lines correspond to results obtained by a free minimization of the original Rosenfeld functional. The simulation data ($\square$) are taken from Ref. [10]. As in Fig. 1 the positions of the extrema of $\rho_s(z)$ and $\rho_b(z)$ are very close to each other if they are measured from the corresponding position of contact, i.e., $z = R_s = \frac{1}{2}\sigma_s$ and $z = R_b = \frac{3}{2}\sigma_s$, respectively. The dotted lines correspond to the coarse grained density profiles defined in Eq. (23). Different from Fig. 1, here the net density of both species is clearly enhanced near the wall.

be able to resolve these small differences magnified parts of the density profiles from Fig. 1 are shown in Fig. 3 together with the simulation data from Ref. [10] ($\square$). The solid lines in Fig. 3 correspond to the original Rosenfeld functional, the dotted lines correspond to the interpolated version [Eq. (8)] and the dashed and dash-dotted lines correspond to the anti-symmetrized version [Eq. (7)] with $q = 2$ and 3, respectively. All DFT results are very close to the simulation data. However, the deviations between the simulations and the anti-symmetrized functional with $q = 2$ seem to be systematically the largest.

In Figs. 4 and 5 we show the density profiles of a binary mixture with size ratio $R_b:R_s = 3:1$. The packing fraction of the small spheres is $\eta_s = 0.0047$ and that of the big spheres is $\eta_b = 0.3859$, so that the total packing fraction $\eta = \eta_s + \eta_b = 0.3906$ is again rather high. Therefore, there is a strong spatial variation of the density profiles. The agreement between DFT (solid line) and simulations ($\square$) is again found to be excellent for both the density profile of the small spheres (a) and the big spheres (b). The dotted lines denote the coarse grained densities as defined in Eq. (23) [29]. The
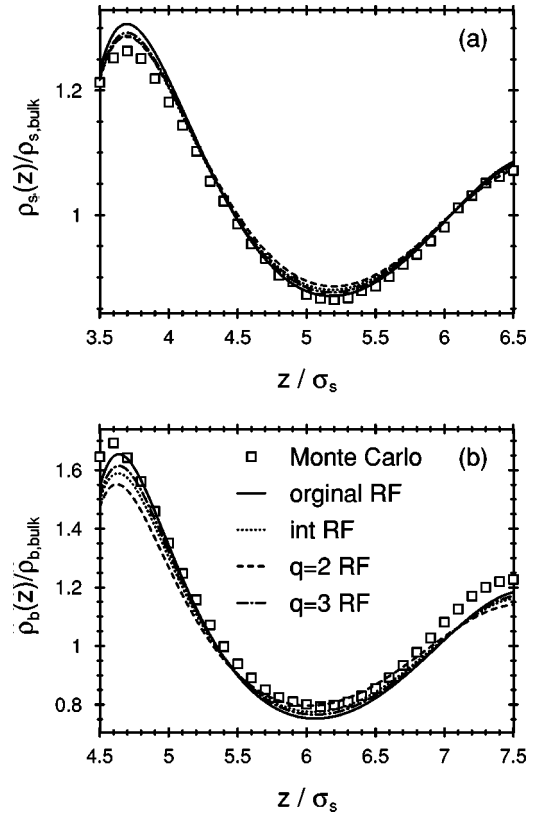
FIG. 5. In order to highlight the small differences of the DFT results obtained by different versions of the Rosenfeld functional, here small parts of the density profiles shown in Fig. 4 are magnified.

concentrations profiles of the small and big spheres, corresponding to these density profiles, are shown in Fig. 6. For this larger size ratio the anticorrelated behavior of $\Phi_s(z)$ and $\Phi_b(z)$ is even more pronounced than for the smaller ratio discussed in Fig. 2, and strongly locked in without additional fine structure such as the double peak appearing in Fig. 2.
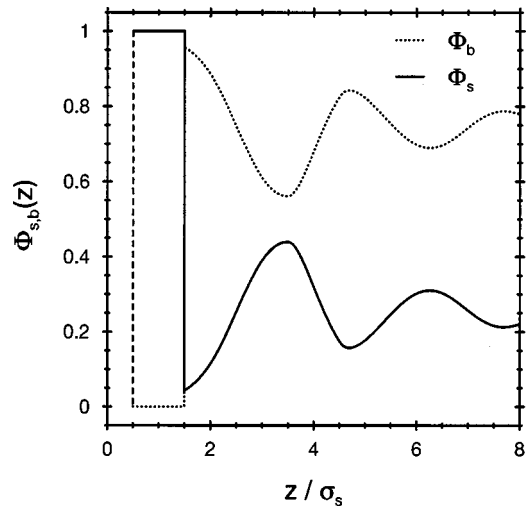

FIG. 6. The concentration profiles $\Phi_s(z)$ and $\Phi_b(z)$ of the small and big spheres, respectively, corresponding to the density profiles of Fig. 4. $R_s = \frac{1}{2}\sigma_s$ and $R_b = \frac{3}{2}\sigma_s$, so that, due to geometric constraints, $\Phi_b(R_s < z < R_b) = 0$ and $\Phi_s(R_s < z < R_b) = 1$. The anticorrelated behavior of the two profiles is strongly locked in.

TABLE I. Contact values at a planar hard wall of a binary hard-sphere mixture with size ratio $R_b:R_s$ $=5:3$ for packing fractions η_s and η_b. The comparison of the sum of the contact values with the Percus-Yevick compressibility equation of state, which underlies the Rosenfeld functional, tests the accuracy of our numerical procedures. For small total packing fractions $\eta=\eta_s+\eta_b$ this equation of state is in good agreement with the more accurate equation of state βp_{MCSL} established by Mansoori et al. [31]. However, for larger values of η, there are deviations.

η	η_s	η_b	$R_s^3\Sigma_i\rho_i(R_i+0)$	$R_s^3\beta p_{PY}^c$	$R_s^3\beta p_{MCSL}$
0.1246	0.0246	0.1000	0.01804	0.01804	0.01801
0.1252	0.0880	0.0372	0.03809	0.03809	0.03805
0.1309	0.0026	0.1283	0.01256	0.01256	0.01253
0.1850	0.0990	0.0890	0.06116	0.06116	0.06089
0.2005	0.0356	0.1649	0.03901	0.03901	0.03877
0.2247	0.0126	0.2121	0.03697	0.03698	0.03670
0.2278	0.1812	0.0466	0.12304	0.12306	0.12202
0.2670	0.1953	0.0717	0.16351	0.16354	0.16132
0.2749	0.0545	0.2204	0.07985	0.07987	0.07878
0.3477	0.0257	0.3220	0.11401	0.11405	0.11097
0.3712	0.0607	0.3105	0.16908	0.16916	0.16372
0.3906	0.0058	0.2984	0.06845	0.06847	0.06713
0.3968	0.0120	0.3848	0.15642	0.15652	0.15018

In addition we test the numerical accuracy of our calculations by means of the sum rule given in Eq. (20). In Table I the sum of the contact values of the binary mixture with size ratio $R_b:R_s=5:3$ for various packing fractions is compared with two equations of state. βp_{PY}^c denotes the Percus-Yevick compressibility equation of state [Eq. (19)], to which the Rosenfeld functional reduces in the bulk limit, and βp_{MCSL} corresponds to the more accurate Mansoori-Carnahan-Starling-Leland equation of state [31], which represents a generalization to a mixture of the very accurate Carnahan-Starling equation of state [32] for the one-component fluid. The very good agreement between the contact values and βp_{PY}^c demonstrates the high accuracy of our numerical procedure. However, at higher packing fractions, βp_{PY}^c deviates from the more accurate equation of state βp_{MCSL}. The same analysis of our results for a binary mixture with size ratio $R_b:R_s=3:1$ is summarized in Table II.

Equation (20) represents a sum rule which must be fulfilled by the density profiles as obtained by any of the density functionals considered here. However, no corresponding rules are available for the individual contact values. We find

that for all versions of the Rosenfeld functional under consideration here, the sum rule is respected equally well. However, the individual contact values may differ. This statement is in line with the expectation that the greatest differences between the various versions of the Rosenfeld functional occur in a region where ξ is large, i.e., close to the wall, and is substantiated in Table III for the binary mixture with size ratio $R_b:R_s=5:3$ and in Table IV for the size ratio $R_b:R_s$ $=3:1$.

Vested with this confidence in our numerical procedures and the excellent agreement in all details between our DFT density profiles and the simulation data from Ref. [10], we are now able to draw the conclusion that the Rosenfeld functional predicts the structure of the density profiles of a binary hard-sphere mixture near a planar wall with quantitative reliability; it exhibits the same high accuracy as in the case of the one-component hard-sphere fluid. This holds for all versions of the functional considered here, including the DFT due to Kierlik and Rosinberg, which was applied in Ref. [10], and is demonstrated by Figs. 1 and 3–5 and the very small values of the mean square deviations $\bar{E}_s$ and $\bar{E}_b$ [Eq.

TABLE II. Results for the same quantities as in Table I for a binary hard-sphere mixture with size ratio $R_b:R_s=3:1$.

η	η_s	η_b	$R_s^3\Sigma_i\rho_i(R_i+0)$	$R_s^3\beta p_{PY}^c$	$R_s^3\beta p_{MCSL}$
0.1209	0.0188	0.1021	0.00778	0.00778	0.00776
0.1288	0.0037	0.1251	0.00313	0.00313	0.00313
0.1456	0.0283	0.1173	0.01219	0.01219	0.01219
0.2230	0.0026	0.2204	0.00643	0.00643	0.00637
0.2471	0.0199	0.2272	0.01590	0.01590	0.01578
0.2513	0.0089	0.2424	0.01104	0.01104	0.01094
0.3021	0.0016	0.3005	0.01180	0.01180	0.01159
0.3257	0.0136	0.3121	0.02166	0.02166	0.02124
0.3775	0.0099	0.3676	0.02837	0.02837	0.02747
0.3906	0.0047	0.3859	0.02718	0.02719	0.02620

TABLE III. Individual contact values of the density profiles for a binary mixture with size ratio $R_b:R_s$ = 5:3 as obtained by the original Rosenfeld functional $[\sigma_i^3\rho_i^{org}(z=R_i+0)]$, the antisymmetrized modification with $q=3$ $[\sigma_i^3\rho_i^{q=3}(z=R_i+0)]$, and the interpolating modification $[\sigma_i^3\rho_i^{int}(z=R_i+0)]$ with $i=s,b$. $\sigma_i=2R_i$ is the diameter of species i. While all versions of the functional respect the sum rule in Eq. (20), the individual contact values differ slightly for the different versions of the DFT. $\eta=\eta_s+\eta_b$ is the total packing fraction.

η	$\sigma_s^3\rho_s^{org}(R_s+)$	$\sigma_s^3\rho_s^{q=3}(R_s+)$	$\sigma_s^3\rho_s^{int}(R_s+)$	$\sigma_b^3\rho_b^{org}(R_b+)$	$\sigma_b^3\rho_b^{q=3}(R_b+)$	$\sigma_b^3\rho_b^{int}(R_b+)$
0.1246	0.07051	0.07058	0.07059	0.34182	0.34150	0.34144
0.1252	0.27332	0.27340	0.27343	0.14522	0.14487	0.14478
0.1309	0.00745	0.00746	0.00746	0.43082	0.43077	0.43077
0.1850	0.38587	0.38639	0.38657	0.47860	0.47619	0.47550
0.2005	0.13385	0.13432	0.13444	0.82502	0.82284	0.82229
0.2247	0.05002	0.05036	0.05043	1.13782	1.13628	1.13594
0.2278	0.90612	0.90702	0.90727	0.36210	0.35787	0.35677
0.2670	1.15640	1.15871	1.15943	0.70205	0.69099	0.68829
0.2749	0.27715	0.27944	0.28026	1.67448	1.66398	1.65994
0.3477	0.17094	0.17520	0.17709	3.43107	3.41124	3.40174
0.3712	0.47247	0.48279	0.48746	4.07483	4.02673	4.00460
0.3906	0.03099	0.03160	0.03181	2.39204	2.38927	2.38826
0.3968	0.10016	0.10471	0.10703	5.33002	5.30870	5.29677

(22)]. Our calculations clearly confirm the equivalence of the original Rosenfeld functional and the DFT due to Kierlik and Rosinberg, which was proven in Ref. [22] in general terms. This observation provides additional confidence in the reliability of our numerical procedures.

Therefore, the doubts raised in Ref. [10] about the performance of the Rosenfeld DFT for binary hard-sphere mixtures are not justified. In contrast to our results, the density profiles of the small spheres shown in Ref. [10] display breaks in slope and are out of phase compared with the simulation data (see Figs. 5–8 in Ref. [10]). There is strong evidence that in particular the density profiles for the size ratio $R_b:R_s=3:1$ shown in Ref. [10] violate the sum rule given by Eq. (20). Both deficiencies are most likely due to numerical problems. Unfortunately, the numerical accuracy of the results published in Ref. [10] is not documented. Finally we want to mention that earlier studies of binary hard-sphere mixture [8,9,11–15] using DFT approaches different from the Rosenfeld functional yield only qualitatively correct density profiles.

B. Excess adsorption and surface tension

One of the virtues of DFT is that based on the knowledge of the local structural properties $\rho_i(z)$, $i=s,b$, it is also straightforward to calculate thermodynamic properties such as the excess adsorptions Γ_i and the surface tension γ. Here we determine these quantities near a hard wall for a binary hard-sphere fluid whose components exhibit a size ratio $R_b:R_s=3:1$. Our analysis is confined to the fluid phase of the mixture; the phase boundary for freezing is estimated from the bulk phase diagrams presented in Refs. [33].

The excess adsorption of species i, $i=s,b$, is defined as

$$\Gamma_i=\int_0^\infty dz(\rho_i(z)-\rho_{i,bulk}),$$

$$=\int_{\sigma_i/2}^\infty dz(\rho_i(z)-\rho_{i,bulk})-\frac{\sigma_i}{2}\rho_{i,bulk}. \qquad (24)$$

This definition of the excess adsorption differs from the defi-

TABLE IV. Results for the same quantities as in Table III for a binary mixture with size ratio $R_b:R_s$ = 3:1.

| η	$\sigma_s^3\rho_s^{org}(R_s+)$	$\sigma_s^3\rho_s^{q=3}(R_s+)$	$\sigma_s^3\rho_s^{int}(R_s+)$	$\sigma_b^3\rho_b^{org}(R_b+)$	$\sigma_b^3\rho_b^{q=3}(R_b+)$	$\sigma_b^3\rho_b^{int}(R_b+)$
0.1209	0.04862	0.04864	0.04864	0.36808	0.36769	0.36761
0.1288	0.00932	0.00933	0.00932	0.42401	0.42387	0.42389
0.1456	0.07891	0.07895	0.07895	0.50360	0.50248	0.50231
0.2230	0.00839	0.00842	0.00841	1.16319	1.16241	1.16248
0.2471	0.07074	0.07101	0.07104	1.52497	1.51744	1.51686
0.2513	0.03121	0.03136	0.03136	1.54220	1.53814	1.53814
0.3021	0.00626	0.00633	0.00633	2.37903	2.37714	2.37714
0.3257	0.05996	0.06072	0.06078	3.05954	3.03862	3.03744
0.3775	0.05168	0.05289	0.05299	4.73342	4.69975	4.69719
0.3906	0.02540	0.02612	0.02617	5.18598	5.16579	5.16450
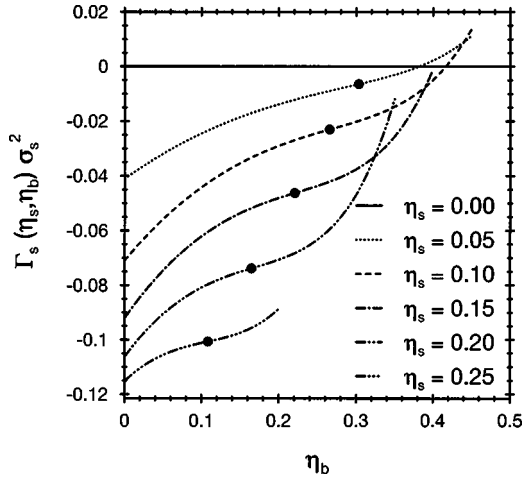
FIG. 7. The excess adsorption Γ_s of the small spheres near a planar hard wall as a function of the packing fractions η_s and η_b in the fluid phase [37]. The dots (●) denote turning points.

FIG. 8. The excess adsorption Γ_b of the big spheres near a planar hard wall as a function of the packing fractions η_s and η_b in the fluid phase [37]. The dots (●) denote turning points. The square symbols (□) denote simulation results for the excess adsorption of a one-component hard-sphere fluid taken from Ref. [35].

nition used in Ref. [34], as well as from that used in Ref. [35]. To recover the results for the excess adsorption of a one-component hard-sphere fluid in Refs. [34] and [35], one has to subtract from and add to our results, respectively, the constant $(\sigma_i/2)\rho_{i,bulk}$. These differences originate from different choices for the position of the wall. While for the one-component fluid there is no preference for any of these definitions, our choice used here appears to be particularly suited for a mixture because, independent of the diameter σ_i of species i, the integrals in Eq. (24) start at the same lower bound for all species, namely, at the position of the physical wall. We use the same definition for the position of the wall to determine the surface tension. Because the excess adsorptions follow from integrating over oscillatory functions, they depend very sensitively on the precise structure of the density profiles and require very accurate calculations. Moreover, near the phase boundary for freezing the original Rosenfeld functional yields values for Γ_s and Γ_b which differ significantly from those obtained from the modifications of the Rosenfeld functional. Thus, unless stated otherwise, we have determined the excess adsorption by using a modified Rosenfeld functional corresponding to Eq. (8), which is known to capture the freezing transition of the one-component hard-sphere fluid.

In Fig. 7 we show the excess adsorptions Γ_s of the small spheres as function of the packing fractions η_s and η_b; note that $\Gamma_s(\eta_s=0,\eta_b)\equiv0$. For a fixed packing fraction of the small spheres η_s, the excess adsorption of the small spheres increases upon increasing η_b. The reason for this is that the increasing packing effects of the big spheres associated with large values of η_b enforces also the packing of the small spheres, giving rise to a strongly enhanced contact value and very pronounced structures in the density profile of the small spheres. For very small η_s, i.e., $\eta_s\lesssim0.1$, and large η_b we find that Γ_s can become positive. As a function of η_b, Γ_s exhibits a turning point for any fixed value of η_s.

The excess adsorption Γ_b of the big spheres is shown in Fig. 8. For constant η_s and increasing η_b, Γ_b decreases. But due to the same mechanism as described above, Γ_b increases upon increasing η_s for constant packing fractions of the big spheres η_b. The square symbols (□) in Fig. 8 denote simu-

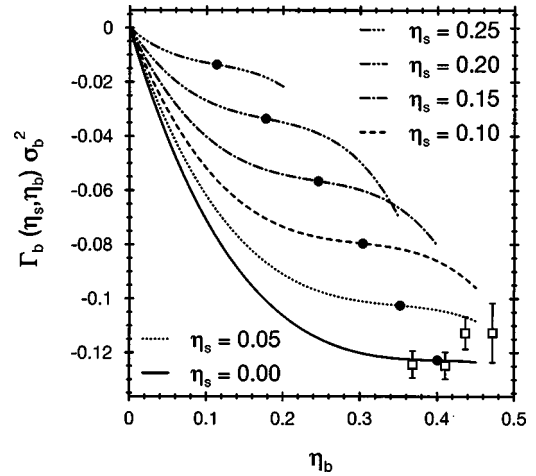lation data for the excess adsorption of a one-component hard-sphere fluid near a hard wall at packing fractions η_s = 0.3680, 0.4103, 0.4364, and 0.4719, respectively, taken from Ref. [35]. Whereas the simulation data for the two smaller packing fractions agree very well with our DFT results, those for the higher values of η_s clearly deviate from the DFT prediction. We note that neither the modified DFT nor the original Rosenfeld DFT predicts the pronounced minimum close to freezing in the excess adsorption of the one-component fluid, as predicted by a fit to the simulation data of Ref. [35] [see Eq. (50) in Ref. [35]] or by the excess adsorption calculated by using the quasiexact surface tension given in Ref. [36]. The origin of this difference is not yet clear. It might reflect the fact that the bulk thermodynamics underlying the Rosenfeld functional is the Percus-Yevick theory with its known deficits near freezing. However, one should keep in mind that the error bars of the simulations are large enough to allow for the absence of this minimum.

In order to illustrate the large differences between the excess adsorptions calculated from different functionals, in Fig. 9 we show the excess adsorptions Γ_s and Γ_b calculated from the original Rosenfeld functional together with those calculated by using the modified functional corresponding to Eq. (8). The packing fraction of the small spheres is η_s = 0.15. Only for small packing fractions of the big spheres, i.e., far away from freezing, do we find good agreement between the results obtained from the different functionals. Close to the phase boundaries [37] the differences become large, which is indeed surprising at first glance. However, the main contribution of the excess adsorption stems from the vicinity of the wall where ξ is large, and the different versions of the Rosenfeld functional are expected to differ. These differences were already indicated in Sec. III A by the behavior of the individual contact values $\sigma_i^3\rho_i(R_i+0)$, i $=s,b$, of the density profiles of the small and big spheres, respectively. For large distances from the wall the density profiles exhibit decaying oscillations, and therefore are not expected to contribute essentially to the excess adsorption. Moreover, *all* versions of the Rosenfeld functional display a
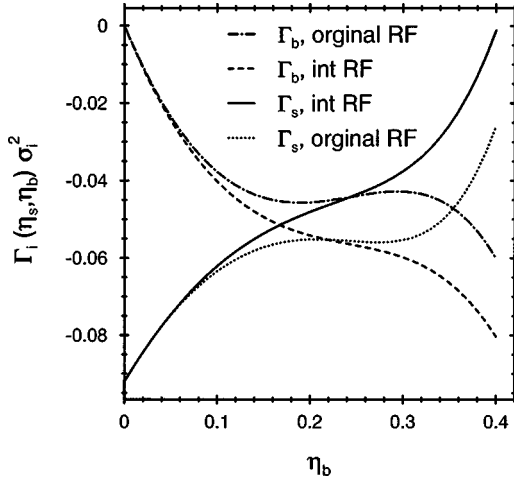
FIG. 9. Excess adsorptions Γ_s and Γ_b calculated with the original Rosenfeld functional compared with those obtained from its modification corresponding to Eq. (8). The packing fraction of the small spheres is $\eta_s = 0.15$.

common characteristic decay because they share the same bulk properties [23], so that the contributions to the excess adsorption far away from the wall are very similar for the original Rosenfeld functional and its modifications.

The grand potential Ω of a system in contact with a wall,

$$\Omega = \Omega_{bulk} + \Omega_{surf}, \qquad (25)$$

decomposes into a bulk contribution $\Omega_{bulk} = -pV$, given by the bulk pressure p in the system times the volume V occupied by fluid particles, and a surface contribution $\Omega_{surf} = \gamma A$, which is the surface tension γ times the surface area A of the wall. Scaled particle theory (SPT) provides an approximate expression for γ for a one-component hard-sphere fluid [38] as well as a generalization to hard-sphere mixtures [24] close to a planar hard wall. The surface tension of a one-component hard-sphere fluid within SPT is well tested, and turns out to provide reliable results as compared with both DFT calculations [34] and simulations [39]. In Ref. [36] a fit to simulation results of the surface tension of a one-component hard-sphere fluid at a planar hard wall is presented, which gives quasiexact results, and closely resembles the SPT expression.

In terms of the weighted bulk densities $n_0, \ldots, n_3$, defined in Eqs. (15)–(18), the SPT approximation for the surface tension of a hard-sphere mixture close to a planar hard wall [24] can be written as

$$\beta\gamma_{SPT} = \frac{n_1}{1-n_3} + \frac{1}{8\pi} \frac{n_2^2}{(1-n_3)^2}. \qquad (26)$$

This expression reduces to the one-component SPT approximation of the surface tension when it is evaluated for the one-component bulk weighted densities. In this latter case the surface tension can be expressed solely in terms of the packing fraction η of this single component.

Within the Rosenfeld functional the surface tension γ of a binary hard-sphere mixture at a planar hard wall follows from the equilibrium density profiles $\rho_i(z)$, $i = s, b$, as obtained in Sec. III A:
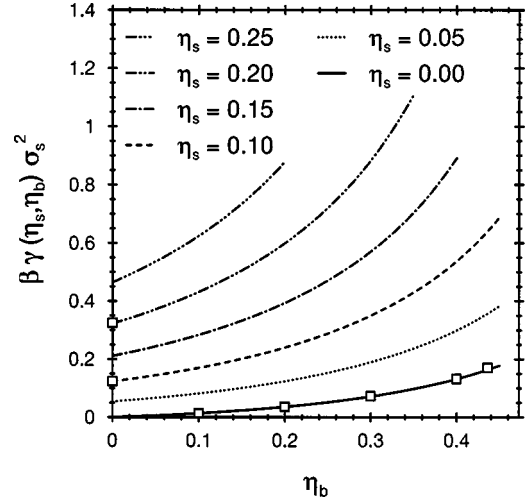

FIG. 10. The surface tension $\beta\gamma(\eta_s, \eta_b)$ of a binary hard-sphere mixture in the fluid phase [37] with size ratio $R_b : R_s = 3 : 1$ as function of the packing fractions η_s and η_b, calculated from the original Rosenfeld functional (lines). For $\eta_s = 0$ the hard-sphere fluid freezes at $\eta_b = 0.494$. The square symbols ($\square$) denote simulation results from Ref. [39] for the one-component hard-sphere fluid.

$$\beta\gamma = \frac{\beta\Omega + \beta pV}{A}$$

$$= \lim_{L \to \infty} \left[\beta pL + \int_0^L dz \left\{ \Phi[\rho_s(z), \rho_b(z)] \right. \right.$$

$$\left. \left. + \sum_{i=s,b} \rho_i(z)(V_{ext}^i(z) - \mu_i) \right\} \right]. \qquad (27)$$

In contrast to the strong dependence of the results of the excess adsorption on the choice of functional, we find that the original Rosenfeld functional as well as its modifications predict very similar results for the surface tension in the whole range of packing fractions studied here. Our results for the surface tension of a binary hard-sphere mixture with size ratio $R_b : R_s = 3 : 1$, calculated within the original Rosenfeld functional, are shown in Fig. 10. The deviation between these results and those obtained by the modifications of the Rosenfeld functional are at most 3%, and deviate from the predictions of the SPT at most by 10%.

IV. SUMMARY AND CONCLUSIONS

Based on the Rosenfeld density functional we have analyzed structural and thermodynamic properties of binary hard-sphere mixtures near a hard wall, with the following main results.

(1) Figures 1 and 4 demonstrate that the structures of both density profiles $\rho_i(z)$, $i = s, b$, of a binary hard-sphere mixture close to a planar hard wall, as obtained by the original Rosenfeld functional, are in excellent agreement with simulation results for size ratios $R_b : R_s = 5 : 3$ and $R_b : R_s = 3 : 1$, respectively. The high level of agreement between our DFT results and the simulation data from Ref. [10] is confirmed quantitatively by small mean square deviations $\bar{E}_s$ and $\bar{E}_b$ defined in Eq. (22). In terms of these quantities all versions

of the Rosenfeld functional are practically of the same quality. Only at high packing fractions do rather small differences between the results obtained by different versions of the Rosenfeld DFT become visible, like those shown in Figs. 3 and 5.

(2) The concentration profiles (see Figs. 2 and 6) calculated from the density profiles confirm the depletion picture: the small spheres are depleted from regions close to the wall, while the big spheres are enriched.

(3) The numerical accuracy of our calculations is demonstrated in Tables I and II by the high degree at which the sum rule Eq. (20), which relates the sum of the contact values of both density profiles with the equation of state, is respected. The sum rule, however, makes no prediction for the individual contact values and we find in Tables III and IV that each version of the Rosenfeld functional takes a different route to satisfy the sum rule.

(4) Using the modified Rosenfeld functional corresponding to Eq. (8), we have calculated the excess adsorption of the small spheres $\Gamma_s(\eta_s, \eta_b)$ (see Fig. 7) and of the big spheres $\Gamma_b(\eta_s, \eta_b)$ (see Fig. 8) as functions of the packing fractions η_s and η_b for a binary hard-sphere mixture with a size ratio $R_b : R_s = 3:1$. We find that these quantities depend very sensitively on the accuracy of the numerical calculations and, as can be seen in Fig. 9, they differ significantly from the excess adsorption calculated by the original Rosenfeld functional.

(5) The surface tension of a binary hard-sphere mixture with size ratio $R_b : R_s = 3:1$ close to a planar hard wall is shown in Fig. 10. We find that all versions of the Rosenfeld functional give results which are in good agreement with the prediction of scaled particle theory [Eq. (26)].

From these results we conclude that the class of Rosenfeld functionals yields quantitatively reliable descriptions of interfacial structures in binary hard-sphere fluids. We expect that the same level of reliability also holds for multicomponent hard-sphere fluids.

The excess adsorptions Γ_s and Γ_b of the small and big spheres emphasize the differences between the various versions of the Rosenfeld functional most. In order to decide whether the original Rosenfeld functional or whether its modifications predict these quantities more accurately, additional simulation data of the excess adsorption in a binary hard-sphere fluid are needed.

APPENDIX: CALCULATION OF THE WEIGHTED DENSITIES

Within the minimization procedure of the Rosenfeld functional the weighted densities n_α and $\mathbf{n}_\alpha$ have to be calculated repeatedly. Therefore, it is necessary to optimize these calculations with respect to both computational speed and numerical accuracy.

The weight functions of the Rosenfeld functional are given by

$$\omega_i^{(3)}(\mathbf{r}) = \Theta(|\mathbf{r}| - R_i), \tag{A1}$$

$$\omega_i^{(2)}(\mathbf{r}) = \delta(|\mathbf{r}| - R_i), \tag{A2}$$

and

$$\boldsymbol{\omega}_i^{(2)}(\mathbf{r}) = \frac{\mathbf{r}}{|\mathbf{r}|} \delta(|\mathbf{r}| - R_i), \tag{A3}$$

with the Heaviside function Θ and the Dirac delta function δ. The remaining scalar weight functions are proportional to $\omega_i^{(2)} : \omega_i^{(1)} = \omega_i^{(2)}/(4\pi R_i)$ and $\omega_i^{(0)} = \omega_i^{(2)}/(4\pi R_i^2)$. The first vector weight function is collinear with $\boldsymbol{\omega}_i^{(2)} : \boldsymbol{\omega}_i^{(1)} = \boldsymbol{\omega}_i^{(2)}/(4\pi R_i)$.

In order to calculate the weighted densities, integrals $I_i^{(\alpha)}$ of the type

$$I_i^{(\alpha)} = \int d^3 r' \rho_i(\mathbf{r}) \omega_i^\alpha(\mathbf{r} - \mathbf{r}') \tag{A4}$$

have to be evaluated. For these convolution type integrals one can exploit the symmetry properties of the density profiles. For the present geometry the weighted densities can be written as

$$n_\alpha(z) = \sum_{i=s,b} \int_{-R_i}^{R_i} dz' \rho_i(z + z') \bar{\omega}_i^{(\alpha)}(z'), \tag{A5}$$

with s and b for small and big, respectively, and with *reduced* weight functions $\bar{\omega}_i^{(\alpha)}$ which are functions of z only:

$$\bar{\omega}_i^{(3)}(z) = \pi(R_i^2 - z^2), \tag{A6}$$

$$\bar{\omega}_i^{(2)}(z) = 2\pi R_i, \tag{A7}$$

and

$$\bar{\boldsymbol{\omega}}_i^{(2)}(z) = 2\pi z \mathbf{e}_z, \tag{A8}$$

with the unit vector $\mathbf{e}_z$ in the z direction. The relations between these and the remaining weight functions are the same as for the original weight functions. The integrals in Eq. (A5) are one-dimensional convolutions which can be calculated faster and more accurately in Fourier space than in real space. By introducing the Fourier transforms of the density profiles,

$$\hat{\rho}_i(k) = \mathcal{FT}(\rho_i(z)), \tag{A9}$$

and those of the weight functions,

$$\hat{\omega}_i^{(\alpha)}(k) = \mathcal{FT}(\bar{\omega}_i^{(\alpha)}(z)), \tag{A10}$$

the weighted densities can be expressed as

$$n_\alpha(z) = \mathcal{FT}^{-1}\left(\sum_{i=s,b} \hat{\rho}_i(k) \hat{\omega}_i^\alpha(k) \right). \tag{A11}$$

This route of calculation offers the important advantage that the numerical calculation of these convolutions can be sped up significantly by applying fast-Fourier-transform (FFT) methods. Moreover it turns out that calculations of convolutions in real space depend more sensitively on the grid size Δz to be used for discretization than those in Fourier space. We expect that the reason for this is that the FFT algorithm interpolates between data points with trigonometrical func-

tions. To overcome this problem in real space a sophisticated integration scheme would have to be applied or a very small grid size would have to be chosen. Both remedies additionally slow down the numerical calculation in real space.

The results presented in this appendix are applicable if the density profiles depend on the z coordinate only. However, similar results can be obtained if the density profiles have radial symmetry.

---

[1] P. N. Pusey, in *Liquids, Freezing and the Glass Transition*, edited by J.-P. Hansen, D. Levesque, and J. Zinn-Justin (Elsevier, Amsterdam, 1991), p. 763; W. Poon, P. Pusey, and H. Lekkerkerker, Phys. World **9**, 27 (1996).

[2] J.-P. Hansen and I. R. McDonald, *Theory of Simple Liquids*, 2nd ed. (Academic, London, 1986).

[3] R. Evans, Adv. Phys. **28**, 143 (1979); in *Fundamentals of Inhomogeneous Fluids*, edited by D. Henderson (Dekker, New York, 1992); H. Löwen, Phys. Rep. **237**, 249 (1994).

[4] Y. Rosenfeld, Phys. Rev. Lett. **63**, 980 (1989).

[5] R. D. Groot, N. M. Faber, and J. P. van der Eerden, Mol. Phys. **62**, 861 (1987).

[6] I. Pagonabarraga, M. E. Cates, and G. J. Ackland, Phys. Rev. Lett. **84**, 911 (2000).

[7] Z. Tan, U. M. B. Marconi, F. van Swol, and K. E. Gubbins, J. Chem. Phys. **90**, 3704 (1989).

[8] M. Moradi and G. Rickayzen, Mol. Phys. **66**, 143 (1989).

[9] S. Sokołowski and J. Fischer, Mol. Phys. **70**, 1097 (1990).

[10] J. P. Noworyta, D. Henderson, S. Sokołowski, and K.-Y. Chan, Mol. Phys. **95**, 415 (1998).

[11] A. R. Denton and N. W. Ashcroft, Phys. Rev. A **44**, 8242 (1991).

[12] R. Leidl and H. Wagner, J. Chem. Phys. **98**, 4142 (1993).

[13] C. N. Patra, J. Chem. Phys. **111**, 6573 (1999).

[14] N. Choudhury and S. K. Ghosh, J. Chem. Phys. **110**, 8628 (1999).

[15] S.-C. Kim, C. H. Lee, and B. S. Seong, Phys. Rev. E **60**, 3413 (1999).

[16] S.-C. Kim, S.-H. Suh, and C. H. Lee, J. Korean Phys. Soc. **35**, 350 (1999).

[17] Y. Rosenfeld, M. Schmidt, H. Löwen, and P. Tarazona, J. Phys.: Condens. Matter **8**, L577 (1996).

[18] Y. Rosenfeld, M. Schmidt, H. Löwen, and P. Tarazona, Phys. Rev. E **55**, 4245 (1997).

[19] Y. Rosenfeld, in *New Approaches to Problems in Liquid State Theory*, edited by C. Caccamo, J.-P. Hansen, and G. Stell (Kluwer, Dordrecht, 1999), p. 303.

[20] Y. Rosenfeld, J. Chem. Phys. **98**, 8126 (1993).

[21] E. Kierlik and M. L. Rosinberg, Phys. Rev. A **42**, 3382 (1990).

[22] S. Phan, E. Kierlik, M. L. Rosinberg, B. Bildstein, and G. Kahl, Phys. Rev. E **48**, 618 (1993).

[23] R. Evans, R. J. F. Leote de Carvalho, J. R. Henderson, and D. C. Hoyle, J. Chem. Phys. **100**, 591 (1994).

[24] J. L. Lebowitz and J. S. Rowlinson, J. Chem. Phys. **41**, 133 (1964).

[25] G. Rickayzen, Mol. Phys. **55**, 161 (1985).

[26] F. van Swol and J. R. Henderson, Phys. Rev. A **40**, 2567 (1989).

[27] We denote the packing fraction of the species i in the reservoir by $\eta_i = (4\pi/3) R_i^3 \rho_i$ $(i=s,b)$.

[28] For the density profiles in Fig. 1, we find the following values: $z_s^{(1)} = 1.3276\sigma_s$, $z_s^{(2)} = 2.9603\sigma_s$, $\bar{\rho}_s^{(0)} = 0.9313$, and $\bar{\rho}_s^{(1)} = 0.9719$ for the small spheres, and $z_b^{(1)} = 1.6289\sigma_s$, $z_b^{(2)} = 3.2652\sigma_s$, $\bar{\rho}_b^{(0)} = 0.8873$, and $\bar{\rho}_b^{(1)} = 0.9589$ for big spheres.

[29] For the density profiles in Fig. 4 we find the following values: $z_s^{(1)} = 2.2338\sigma_s$, $z_s^{(2)} = 5.1791\sigma_s$, $\bar{\rho}_s^{(0)} = 1.3217$, and $\bar{\rho}_s^{(1)} = 0.9894$ for the small spheres, and $z_b^{(1)} = 3.1247\sigma_s$, $z_b^{(2)} = 6.0624\sigma_s$, $\bar{\rho}_b^{(0)} = 1.7096$, and $\bar{\rho}_b^{(1)} = 0.9757$ for big spheres.

[30] B. Götzelmann, R. Evans, and S. Dietrich, Phys. Rev. E **57**, 6785 (1998).

[31] G. A. Mansoori, N. F. Carnahan, K. E. Starling, and T. W. Leland, Jr., J. Chem. Phys. **54**, 1523 (1971).

[32] N. F. Carnahan and K. E. Starling, J. Chem. Phys. **51**, 635 (1969).

[33] M. Dijkstra, R. Van Roij, and R. Evans, Phys. Rev. Lett. **81**, 2268 (1998); **82**, 117 (1999); Phys. Rev. E **59**, 5744 (1999).

[34] B. Götzelmann, A. Haase, and S. Dietrich, Phys. Rev. E **53**, 3456 (1996).

[35] J. R. Henderson and F. van Swol, Mol. Phys. **51**, 991 (1984).

[36] D. Henderson and M. Plischke, Proc. R. Soc. London, Ser. A **410**, 409 (1987).

[37] The precise phase boundaries toward freezing of a binary hard-sphere mixture with size ratio $R_b : R_s = 3:1$ are not known. Therefore, we roughly estimated the onset of freezing from the phase diagram of a binary hard-sphere mixture with size ratio $R_b : R_s = 5:1$ [33] to be close to $\eta_b = 0.45$ for $\eta_s \leq 0.1$, $\eta_b = 0.4$ for $\eta_s = 0.15$, $\eta_b = 0.35$ for $\eta_s = 0.2$, and $\eta_b = 0.2$ for $\eta_s = 0.25$.

[38] H. Reiss, H. L. Frisch, E. Helfand, and J. L. Lebowitz, J. Chem. Phys. **32**, 119 (1960).

[39] M. Heni and H. Löwen, Phys. Rev. E **60**, 7057 (1999).